Engineering 12 (2022) 62–69

Contents lists available at ScienceDirect

Engineering

journal homepage: www.elsevier.com/locate/eng

Research
Green Chemical Engineering—Article

Regulation of Oxygen Activity by Lattice Confinement over $Ni_xMg_{1-x}O$ Catalysts for Renewable Hydrogen Production

Hao Tian [a,b], Chunlei Pei [a,b], Sai Chen [a,b], Yang Wu [a,b], Zhijian Zhao [a,b], Jinlong Gong [a,b,c,*]

[a] Key Laboratory for Green Chemical Technology of Ministry of Education, School of Chemical Engineering and Technology, Tianjin University, Tianjin 300072, China
[b] Collaborative Innovation Center of Chemical Science and Engineering, Tianjin 300072, China
[c] Joint School of National University of Singapore and Tianjin University, International Campus of Tianjin University, Binhai New City, Fuzhou 350207, China

ARTICLE INFO

Article history:
Received 2 April 2020
Revised 5 August 2020
Accepted 10 August 2020
Available online 25 February 2022

Keywords:
Chemical looping
Ethanol steam reforming
Nickel
Hydrogen production
Solid solution

ABSTRACT

The chemical looping steam reforming (CLSR) of bioethanol is an energy-efficient and carbon-neutral approach of hydrogen production. This paper describes the use of a $Ni_xMg_{1-x}O$ solid solution as the oxygen carrier (OC) in the CLSR of bioethanol. Due to the regulation effect of Mg^{2+} in $Ni_xMg_{1-x}O$, a three-stage reaction mechanism of the CLSR process is proposed. The surface oxygen of $Ni_xMg_{1-x}O$ initially causes complete oxidation of the ethanol. Subsequently, H_2O and bulk oxygen confined by Mg^{2+} react with ethanol to form CH_3COO^* followed by H_2 over partially reduced $Ni_xMg_{1-x}O$. Once the bulk oxygen is consumed, the ethanol steam reforming process is promoted by the metallic nickel in the stage III. As a result, $Ni_{0.4}Mg_{0.6}O$ exhibits a high H_2 selectivity (4.72 mol H_2 per mole ethanol) with a low steam-to-carbon molar ratio of 1, and remains stable over 30 CLSR cycles. The design of this solid-solution OC provides a versatile strategy for manipulating the chemical looping process.

1. Introduction

The environmental benefit of hydrogen (H_2) as an energy vector stems from its zero carbon footprint [1–4]. However, more than 95% of H_2 is currently produced from fossil fuels worldwide, leading to even more production of carbon dioxide (CO_2) than that produced from the direct use of fossil fuels [5]. Hence, it is necessary to minimize the dependence on fossil fuels and to shift toward renewable and clean resources for hydrogen production [6,7]. Ethanol (C_2H_5OH) is the most widely used liquid fuel made from renewable biomass and has a relatively high H/C ratio, which is desirable for hydrogen production [8]. Ethanol can be reacted directly with water through steam reforming to produce a H_2-rich gas over 3d transition metal catalysts (Eq. (1)) [9]. This process utilizes the raw product of bioethanol, which avoids the energy-consuming distillation separation of the ethanol–water mixture [9–11].

$$C_2H_5OH + 3H_2O \rightarrow 2CO_2 + 6H_2, \quad \Delta H^{\ominus}_{298K} = 173\ kJ{\cdot}mol^{-1} \tag{1}$$

However, ethanol steam reforming is a strongly endothermic reaction. Chemical looping steam reforming (CLSR), as a process intensification technology, can be employed to promote the efficiency of the steam reforming process [12,13]. In the CLSR of ethanol, the oxygen carrier (OC) is first reduced by ethanol in a reforming reactor. For example, when NiO is used as the OC, the redox reaction between C_2H_5OH and NiO is carried out as shown in Eq. (2).

$$C_2H_5OH + 6NiO\ (s) \rightarrow 2CO_2 + 3H_2O + 6Ni\ (s), \quad \Delta H^{\ominus}_{298K} = 150\ kJ{\cdot}mol^{-1} \tag{2}$$

The Ni^{2+} in NiO is reduced to metallic nickel (Ni) with the depletion of oxygen (O). Next, ethanol steam reforming occurs with the catalysis of metallic Ni (Eq. (1)). The thermal decomposition of ethanol is also carried out on the surface of the Ni when the steam-to-carbon ratio (S/C) is low (Eq. (3)):

$$C_2H_5OH \rightarrow C\ (s) + CO + 3H_2, \quad \Delta H^{\ominus}_{298K} = 136\ kJ{\cdot}mol^{-1} \tag{3}$$

All of Eqs. (1)–(3) are endothermic. Ni is then re-oxidized by air in a regeneration reactor (Eq. (4)). The deposited carbon (C) formed during ethanol steam reforming is also gasified (Eq. (5)).

$$Ni\ (s) + 0.5O_2 \rightarrow NiO\ (s), \quad \Delta H^{\ominus}_{298K} = -187\ kJ{\cdot}mol^{-1} \tag{4}$$

* Corresponding author.
E-mail address: jlgong@tju.edu.cn (J. Gong).

https://doi.org/10.1016/j.eng.2020.08.029

$$C\ (s) + O_2 \rightarrow CO_2,\ \Delta H^{\ominus}_{298K} = -395\ kJ{\cdot}mol^{-1} \quad (5)$$

The heat required for endothermic steam reforming can be supplied from the oxidation of OCs (Eq. (4)) and deposited carbon (Eq. (5)) in the regeneration reactor. Therefore, the excess heat required from an external burner can be minimized. The overall reaction of the CLSR of ethanol can be regarded as the sum of ethanol steam reforming and the complete oxidation of ethanol (Eq. (6)).

$$C_2H_5OH + xH_2O + (1.5 - 0.5x)O_2 \rightarrow 2CO_2 + (3 + x)H_2 \quad (6)$$

The OCs, which are normally reducible metal oxides, play essential roles in the CLSR of ethanol. The use of metal oxides instead of gaseous oxygen (O_2) as the OCs help to avoid safety risks during operation [8]. The extra oxygen from the OCs can remarkably reduce the S/C of the CLSR, which may lead to autothermal hydrogen production from renewable feedstock with an appropriate ratio of ethanol to OC. The OCs in chemical looping processes must meet a number of criteria for practical applications [14,15]. They must exhibit long-term redox stability and provide oxygen species with suitable activity [16]. NiO, as an outstanding candidate, has been investigated for use as the OC in various chemical looping processes [17]. Jiang et al. [18] applied NiO/montmorillonite in the CLSR of ethanol and achieved greater than 60% H_2 selectivity in 20 cycles. However, the oxygen release of bulk NiO is too drastic, and the dispersion of the Ni derived from bulk NiO is relatively inadequate for the activation of reactive species and long-term operation, which limits the stability of Ni-based OCs [19–21]. The regulation of the reduction kinetics is the key to obtaining highly dispersed Ni and further promoting the performance of Ni-based OCs.

Due to the similar atomic sizes of Ni^{2+} (69 pm) and Mg^{2+} (72 pm), a substitutional $Ni_xMg_{1-x}O$ solid solution in any proportion ($0 \leq x \leq 1$) can be formed by means of an adequate calcination temperature [22–24]. The Ni–Ni boundary is isolated by the Mg^{2+} in $Ni_xMg_{1-x}O$; thus, the rapid movement of Ni^{2+} is inhibited in the solid solution [25]. The reduction of the solid solution is related to the rate of bulk Ni^{2+} diffusion and can be tuned by the concentration of Ni^{2+} in $Ni_xMg_{1-x}O$ [26]. Huang et al. [27] designed Mg–Ni–Al–O OCs with a solid solution structure and achieved excellent performance in chemical looping combustion. $Ni_xMg_{1-x}O$ shows great potential for chemical looping processes, although the applicability of $Ni_xMg_{1-x}O$ solid solutions as OCs in the CLSR of ethanol remains unclear.

In this work, $Ni_xMg_{1-x}O$ solid solutions with different chemical compositions were synthesized as OCs to investigate the modulation effect of Mg^{2+} on the CLSR of ethanol. With the introduction of Mg^{2+}, the oxygen release of Ni-based OCs was tunable. The relationship between the structural evolution of $Ni_xMg_{1-x}O$ and the mechanism of the surface reaction was investigated. Ethanol–water pulse and H_2-temperature-programmed reduction (TPR) experiments were applied to explore the oxygen release of $Ni_xMg_{1-x}O$. An *in situ* diffuse reflectance infrared Fourier-transform spectroscopy (DRIFTS) experiment was also carried out to determine the changes in intermediates during the CLSR of ethanol.

2. Material and methods

2.1. Preparation of OCs

A series of $Ni_xMg_{1-x}O$ (x = 0.2, 0.4, 0.6, and 0.8) solid solutions was synthesized using a co-precipitation method. Typically, a mixture of $Mg(NO_3)_2{\cdot}6H_2O$ (98%, J&K Scientific Co., Ltd., China) and $Ni(NO_3)_2{\cdot}6H_2O$ (99%, Aladdin Biological Technology Co., Ltd., China) was dissolved in 150 mL of deionized water (18.25 MΩ) with a total metal molarity of 2 $mol{\cdot}L^{-1}$. Then, 100 mL of as-prepared 6 $mol{\cdot}L^{-1}$ NaOH (99%, Aladdin Biological Technology Co., Ltd.) solution was used as the precipitant. The formed precipitate was aged for 12 h, and the products were filtered and washed thoroughly with hot water to remove sodium. The obtained samples were dried in an oven at 125 °C for 24 h, and then calcined at 700 °C in air for 4 h with a heating rate of 10 $°C{\cdot}min^{-1}$. NiO and MgO were also synthesized by the precipitation method for reference.

2.2. Characterization of OCs

The crystalline structures of the samples were measured using powder X-ray diffraction (XRD; Bruker Corp., USA) with a Bruker D8 Focus equipped with Cu Kα radiation (λ = 1.54056 Å, 1 Å = 10^{-10} m). The diffraction angle 2θ ranged from 20° to 80° with a scan speed of 8° per minute. The texture and morphology of the samples were acquired from transmission electron microscopy (TEM) characterization on a JEM-2100F transmission electron microscope (Japan Electronic Materials Corp., Japan) operated at 200 kV. The samples for TEM analysis were sonicated in ethanol and subsequently supported on copper grid-supported transparent carbon foil. The transmission electron microscope was also equipped with an energy-dispersive X-ray spectroscopy (EDS) detector (Ultim Max, Oxford Instruments, UK) for elemental analysis.

The specific surface area and pore volume of the OCs were measured by nitrogen (N_2) adsorption–desorption at −196 °C using a Micromeritics Tristar II 3020 analyzer (Micromeritics Instrument Corp., USA), based on the Brunauer–Emmett–Teller (BET) and Barrett–Joyner–Halenda (BJH) methods, respectively. Before the tests, all the materials were degassed at 300 °C for 3 h. Elemental compositions of the prepared OCs were determined by means of inductively coupled plasma optical emission spectroscopy (ICP-OES) (VISTA-MPX, Varian, UK). Prior to the measurements, the samples were dissolved in HNO_3 solutions.

The reduction behavior of the OCs was determined by H_2-TPR measurement. The experiments were performed on a Micromeritics Autochem II 2920 instrument equipped with a thermal conductivity detector (TCD; Micromeritics Instrumen Corp., USA). In a typical experiment, the sample (100 mg) was pretreated at 300 °C for 1 h under flowing argon (Ar; 30 $mL{\cdot}min^{-1}$). After the sample had cooled to 100 °C, the analysis was carried out in a mixture of 10 vol% H_2 in Ar (30 $mL{\cdot}min^{-1}$) from 100 to 950 °C at 10 $°C{\cdot}min^{-1}$.

To determine the transfer of oxygen species during the CLSR of ethanol, the C_2H_5OH–H_2O mixture and O_2-pulse experiments were measured on a Micromeritics Autochem II 2920 instrument equipped with a Hiden QIC-20 mass spectrometer (Hiden Analytical, USA). Prior to the experiments, all the samples were pretreated *in situ* using a flow of Ar (30 $mL{\cdot}min^{-1}$) at 300 °C for 1 h. Subsequently, pulses of the mixture of C_2H_5OH and H_2O in Ar or 2% O_2 in helium (He) were admitted to the reactor. The loop volume was 0.5031 mL, and the time interval between different pulses was 3 min, excluding the interference of contiguous pulses. The reactor effluent was continuously monitored by the mass spectrometer, and the gas-phase composition was calculated from the mass spectrometer signal at mass-to-charge ratios (m/z) of 44, 31, 29, 28, 27, 18, 16, and 2 for CO_2, C_2H_5OH, acetaldehyde (CH_3CHO), carbon monoxide (CO), ethene (C_2H_4), water (H_2O), methane (CH_4), and H_2, respectively.

To detect the transformation of intermediates in the CLSR process, *in situ* DRIFTS experiments were performed on a Nicolet iS50 spectrometer (Nicolet iS50, Thermo Scientific, USA) equipped with a Harrick Scientific diffuse reflection accessory and a mercury–cadmium–telluride (MCT) detector cooled by liquid N_2. All samples were pretreated at 600 °C under an Ar flow for 0.5 h,

followed by purging with Ar for 1 h, and were then cooled to 400 °C to obtain a background spectrum. This collected spectrum was then subtracted from the sample spectrum for each measurement under CLSR conditions.

The carbon formation on the OCs was characterized by thermogravimetric analysis (TGA; TGS-2A, Yuanbo, China) and temperature-programmed oxidation (TPO). The TGA experiment was carried out by filling 20 mg of OC into an alumina crucible. The temperature and weight change were then recorded when the temperature was increased from 50 to 900 °C with a heating rate of 10 °C·min^{-1} under air flow (50 mL·min^{-1}). The TPO profiles of the spent OCs were obtained from the same apparatus, as described for the C_2H_5OH-pulse experiment. The OC (50 mg) was pretreated at 300 °C for 0.5 h under flowing Ar (30 mL·min^{-1}). After the OC was cooled to 50 °C, a flow rate of 30 mL·min^{-1} of 10 vol% O_2/He was used for oxidation, and the temperature was increased linearly from 50 to 900 °C. The CO_2 in the effluent was monitored and recorded online using a mass spectrometer.

2.3. CLSR evaluation

CLSR tests were conducted in a stainless-steel tubular fixed-bed reactor with an internal diameter of 20 mm and a length of 400 mm. Two grams of OC (20–40 mesh) was used for the CLSR reaction. Prior to the test, the OCs were pretreated at 600 °C for 1 h under pure N_2 (200 mL·min^{-1}). After purging with N_2, the bed was subsequently adjusted to the designed temperature. An ethanol–water mixture with a flow rate of 0.03 mL·min^{-1} and a specific S/C of 1 was fed through a pump (P230, Elite, China) into a heated chamber (200 °C), where the mixture was completely evaporated in a stream of N_2 (100 mL·min^{-1}) to start the CLSR reaction for 1 h. Then, the reactor was heated to the desired oxidation temperature under air flow (200 mL·min^{-1}) to regenerate the OC for 10 min. The gaseous products were analyzed online by an Agilent 490 Micro gas chromatograph. The gas chromatograph consisted of two different channels for gaseous product analysis. Channel 1 was equipped with a 10 m Molecular Sieve 5A column, with Ar used as the carrier gas for the quantification of permanent gases except for CO_2 (H_2, N_2, CO, and CH_4). Channel 2 was equipped with a 10 m PoraPlot Q column, with He used as the carrier gas for the detection of CO_2 and C_1–C_3 hydrocarbons. All the gaseous products were quantified using the micro-machined thermal conductivity detectors (μTCDs) included in each channel. Liquid products were collected and analyzed over an Agilent 7890A gas chromatograph equipped with a flame ionization detector (FID). Possible liquid products including C_2H_5OH, CH_3CHO, and acetone (CH_3COCH_3) were quantified over the FID with a Porapak-Q column using N_2 as the carrier gas. The selectivities (S_i) of the carbon-containing products were calculated by the following:

$$S_i = \frac{[i]}{[CO_2] + [CO] + [CH_4]} \times 100\% \quad (7)$$

where i represents the different species in the products, and [i] represents the molar concentration of i in the products.

The H_2 selectivity (S_{H_2}) was calculated as follows:

$$S_{H_2} = \frac{F_{H_2}}{F_{C_2H_5OH\text{-in}}} \quad (8)$$

where F_{H_2} represents the molar flow rate of hydrogen in the products, and $F_{C_2H_2OH\text{-in}}$ represents the molar flow rate of ethanol in the reactants.

Product distributions (P_i) were calculated as follows:

$$P_i = \frac{[i]}{[H_2] + [CO_2] + [CO] + [CH_4]} \times 100\% \quad (9)$$

3. Results and discussion

3.1. Structural characterization of $Ni_xMg_{1-x}O$

The physicochemical properties of the as-prepared $Ni_xMg_{1-x}O$ are shown in Table 1. The specific surface area characterized by the BET method is in the range of 15–30 m^2·g^{-1}, and the pore volume is in the range of 0.03–0.06 cm^3·g^{-1}. The XRD patterns of NiO, MgO, and $Ni_xMg_{1-x}O$ are shown in Fig. 1(a). NiO, MgO, and $Ni_xMg_{1-x}O$ possess a rock salt structure. The crystalline sizes of $Ni_xMg_{1-x}O$, as calculated by the Scherrer equation, are similar. To show the influence of the content of Ni on the lattice parameter, the XRD patterns in the range of 40°–46° are provided in Fig. 1(b). The (200) peak of $Ni_xMg_{1-x}O$ shifts from 42.8° to 43.2° with increasing Ni content (i.e., from MgO to NiO). The lattice parameter of $Ni_xMg_{1-x}O$ can be calculated from the peak position based on Bragg's law (Table 1). When the lattice parameter of $Ni_xMg_{1-x}O$ is correlated with the content of Ni in $Ni_xMg_{1-x}O$, a linear relationship can be verified (Fig. 1(c)), which indicates the formation of $Ni_xMg_{1-x}O$ solid solutions in the corresponding Ni/Mg proportions [22].

$Ni_{0.4}Mg_{0.6}O$ is selected as an example to observe the morphology of the solid solution. TEM images of $Ni_{0.4}Mg_{0.6}O$ are given in Figs. 1(d)–(f). According to Figs. 1(d) and (e), the particle size of $Ni_{0.4}Mg_{0.6}O$ is in the range of 10–20 nm. No segregated NiO crystals are observed. The (200) plane of $Ni_xMg_{1-x}O$ with a lattice spacing of 4.215 Å can also be measured in Fig. 1(f), which is in accordance with the results of the XRD characterizations. EDS mapping was applied to probe the elemental dispersion. According to Figs. 1(g)–(i), the distribution of Ni, Mg, and O in $Ni_xMg_{1-x}O$ is homogeneous, indicating the formation of a substitutional solid solution of Ni–Mg oxide.

3.2. CLSR of ethanol

To achieve efficient hydrogen production, 400 °C was chosen as the temperature for the CLSR reaction (Fig. S1 in Appendix A). The S/C was set to 1. The selectivities of the carbon-containing products and H_2 are given in Fig. 2(a). As the content of Ni increases, more CH_4 is generated, which is detrimental to H_2 selectivity. This phenomenon can be attributed to the poor dispersion of Ni (Table 1). CO selectivity over $Ni_{0.2}Mg_{0.8}O$ is the highest among various $Ni_xMg_{1-x}O$ solid solutions. The generation of CO hinders the purity of H_2. In this study, $Ni_{0.4}Mg_{0.6}O$ presents the maximum H_2 selectivity of 4.72 mol H_2 per mole ethanol.

We further studied the properties of $Ni_{0.4}Mg_{0.6}O$. The results from the time-on-stream test of ethanol CLSR over $Ni_{0.4}Mg_{0.6}O$ at 400 °C in a single cycle are given in Fig. 2(b). The CLSR of ethanol can be generally divided into three stages based on the changes in the distribution of products. In stage I (from the start of the reaction to 6 min), CO_2 is the main product. Ethanol is completely oxidized by the surface oxygen of $Ni_{0.4}Mg_{0.6}O$. In stage II (from 6 to 33 min), as more Ni^{2+} ions are gradually reduced to metallic Ni, the decomposition of ethanol occurs over the surface of Ni to produce H_2 and CH_4. The selectivity of the gaseous products is then steadily maintained. The selectivity of H_2 reaches its maximum and the CO concentration is suppressed to 1% in stage II. In stage III (after 33 min) the conversion of ethanol and the selectivities of H_2 and CO_2 decrease with the generation of more CO and CH_4. The deactivation of $Ni_{0.4}Mg_{0.6}O$ occurs in this stage.

A cyclic stability test was carried out on $Ni_{0.4}Mg_{0.6}O$. After the CLSR reaction at 400 °C, the reduced $Ni_{0.4}Mg_{0.6}O$ was re-oxidized and the carbon was combusted in the air at 600 °C for 10 min. This process is referred to as the "regeneration step" in our study. One cyclic test constituted 60 min of the CLSR of ethanol and 10 min of regeneration. The performance of $Ni_{0.4}Mg_{0.6}O$ in the cyclic test is

Table 1
Physicochemical properties of the as-prepared $Ni_xMg_{1-x}O$.

Sample	S_{BET} ($m^2 \cdot g^{-1}$)[a]	V_{pore} ($cm^3 \cdot g^{-1}$)[b]	d_{pore} (nm)[c]	$D_{crystallite}$ (nm)[d]	x_{Ni}[f]	$C_{lattice}$ (Å)[g]	Degree of reduction (%)[h]	Oxygen storage capacity ([O]: $mmol \cdot g^{-1}$)[h]	d_{Ni} (%)[i]
$Ni_{0.2}Mg_{0.8}O$	27.9	0.053	7.3	12.7	0.218	4.2090	42	1.8	9.3
$Ni_{0.4}Mg_{0.6}O$	19.9	0.035	7.0	13.6/14.5[e]	0.408	4.2034	67	5.0	6.9
$Ni_{0.6}Mg_{0.4}O$	18.3	0.039	8.0	10.8	0.621	4.1950	72	7.1	4.2
$Ni_{0.8}Mg_{0.2}O$	15.5	0.031	8.2	11.0	0.828	4.1874	78	9.2	2.3

[a] BET specific surface area.
[b] Total pore volume estimated at $p/p_0 = 0.99$.
[c] BJH pore diameter estimated from the adsorption branch.
[d] $D_{crystallite}$: diameter of $Ni_xMg_{1-x}O$ crystallite. Determined from the (200) peak of $Ni_xMg_{1-x}O$ in the XRD patterns.
[e] The former one is for $Ni_xMg_{1-x}O$ before the test and the latter one is for $Ni_xMg_{1-x}O$ after 30 cycles.
[f] x_{Ni}: stoichiometric number of Ni in $Ni_xMg_{1-x}O$. Measured by ICP-OES.
[g] $C_{lattice}$: lattice constant of $Ni_xMg_{1-x}O$. Calculated by the positions of the (200) peaks of $Ni_xMg_{1-x}O$ in the XRD patterns.
[h] The degree of reduction value of $Ni^0/(Ni^0 + Ni^{2+})$ is calculated by $Ni_xMg_{1-x}O$ after the single reaction stage in CLSR, according to the positions of the (220) peaks of $Ni_xMg_{1-x}O$ in the XRD patterns.
[i] d_{Ni}: dispersion of Ni. Measured by the O_2 pulse experiment.

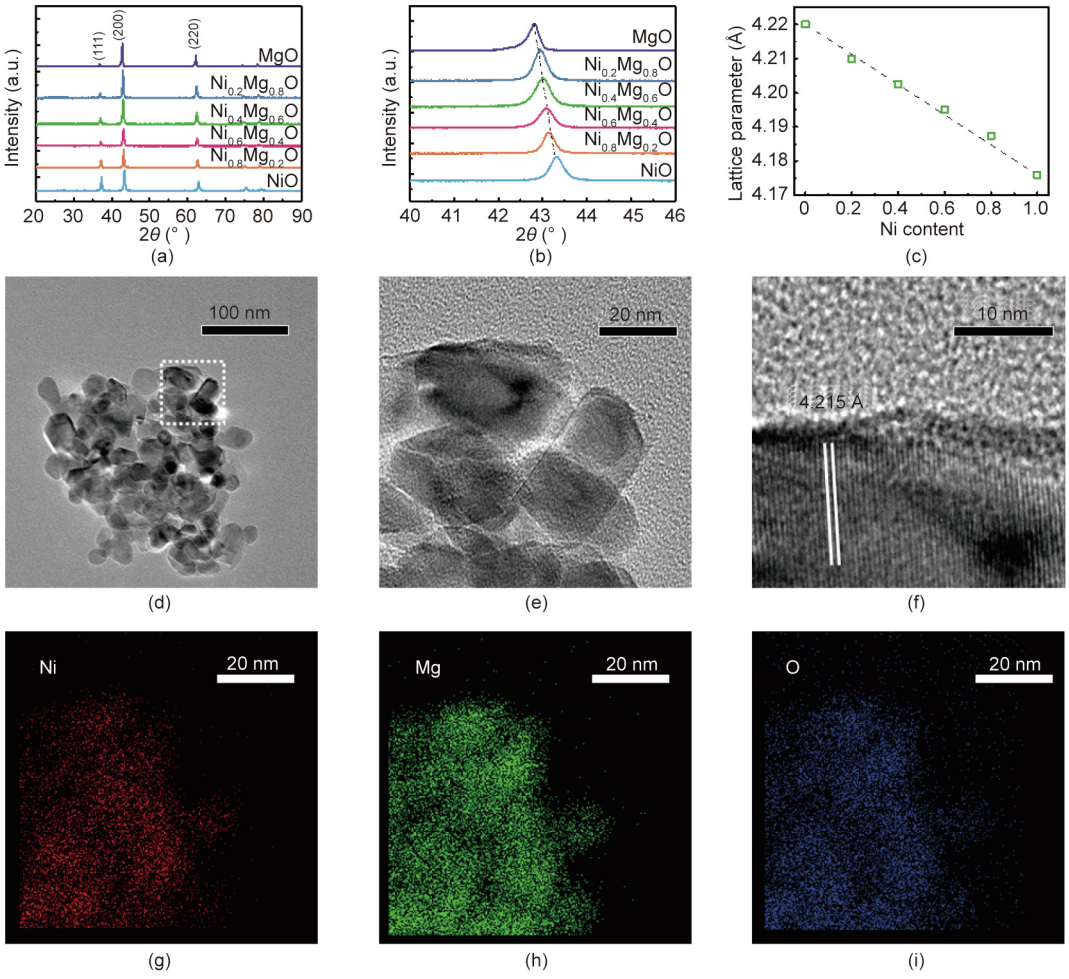

Fig. 1. Crystalline structure and morphology of $Ni_xMg_{1-x}O$. (a) XRD patterns of the as-prepared MgO, $Ni_xMg_{1-x}O$ (x = 0.2, 0.4, 0.6, and 0.8), and NiO. (b) Peaks of the (200) crystal faces of MgO, $Ni_xMg_{1-x}O$, and NiO. (c) Lattice parameters of MgO, $Ni_xMg_{1-x}O$, and NiO calculated from the (200) peaks; the dashed line is the result of a linear fit between lattice parameter and Ni content in $Ni_xMg_{1-x}O$, R^2 = 0.993. (d–f) TEM images of $Ni_{0.4}Mg_{0.6}O$. (g–i) EDS elemental mappings of $Ni_{0.4}Mg_{0.6}O$. a.u.: arbitrary unit.

shown in Fig. 2(c). The selectivity of H_2 over $Ni_{0.4}Mg_{0.6}O$ only drops by about 3% in 30 cycles, indicating that the regeneration can recover the $Ni_{0.4}Mg_{0.6}O$. The structure of $Ni_xMg_{1-x}O$ after 30 cycles was characterized by TEM and XRD (Table 1, Fig. 2(d), and Appendix A Fig. S2). The morphology and crystal structure of $Ni_{0.4}Mg_{0.6}O$ remained the same after the long-term test. The solid-solution OC exists in the form of particles, without the occurrence of sintering. The crystalline size of $Ni_{0.4}Mg_{0.6}O$ after the stability test was 14.2 nm, which is similar to that of fresh $Ni_{0.4}Mg_{0.6}O$. These results verify the recovery of $Ni_{0.4}Mg_{0.6}O$ in the regeneration step and demonstrate the superior stability of this solid solution in the CLSR of ethanol.

3.3. Oxygen release of $Ni_xMg_{1-x}O$

A pulse experiment with an ethanol–water mixture (S/C = 1) over $Ni_{0.4}Mg_{0.6}O$ at 400 °C was conducted in order to explore the oxygen-release process of $Ni_xMg_{1-x}O$ (Fig. 3(a)). During the first

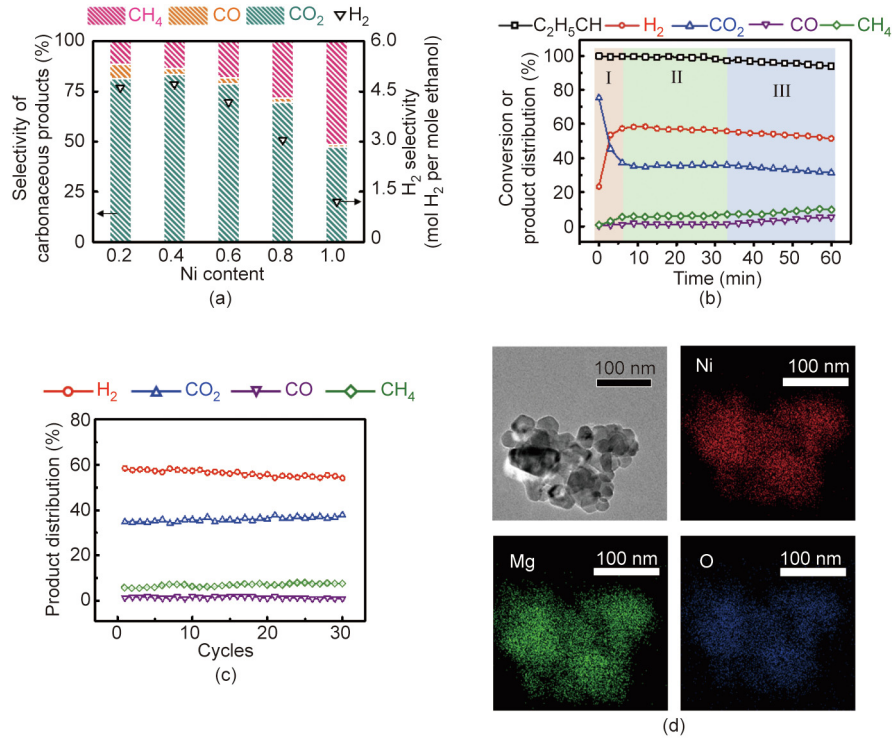

Fig. 2. Performance for the CLSR of ethanol over $Ni_xMg_{1-x}O$. (a) H_2 selectivity and carbon-containing product distribution of different $Ni_xMg_{1-x}O$ solid solutions at 400 °C, during stage II in a single cycle; S/C = 1, ethanol conversion > 95%. (b) Time-on-stream test of $Ni_{0.4}Mg_{0.6}O$ at 400 °C in a single cycle for the CLSR of ethanol. (c) Performance of $Ni_{0.4}Mg_{0.6}O$ in the stability test of 30 cycles. (d) TEM image and EDS elemental mappings of $Ni_{0.4}Mg_{0.6}O$ after 30 cycles of stability testing.

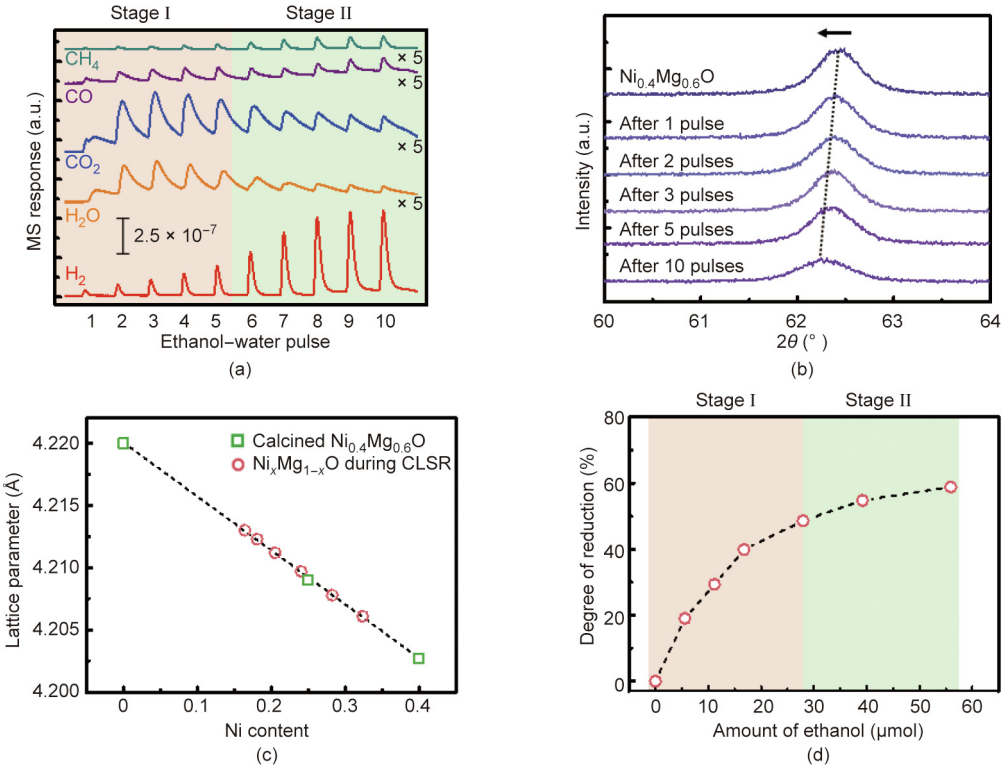

Fig. 3. Oxygen-release behavior of $Ni_{0.4}Mg_{0.6}O$ with ethanol. (a) Ethanol–water mixture pulse experiment on $Ni_{0.4}Mg_{0.6}O$. (b) Peaks of the (220) crystal faces of $Ni_{0.4}Mg_{0.6}O$ during the pulse experiment in XRD patterns. (c) Change in the lattice parameters of $Ni_{0.4}Mg_{0.6}O$ calculated from the (220) peaks during the pulse experiment. (d) Degree of reduction of $Ni_{0.4}Mg_{0.6}O$ during the pulse experiment.

five pulses, the peaks of H_2 were not obvious and CO_2 was the main product. This phenomenon indicates that the redox reaction between $Ni_{0.4}Mg_{0.6}O$ and ethanol is dominant in this period, which corresponds to the stage I observed in the time-on-stream test of $Ni_{0.4}Mg_{0.6}O$ (Fig. 2(b)). Afterward, the H_2 peaks were enlarged and remained stable. CO_2 became the dominant carbonaceous product, which represents the characteristics of stage II.

XRD was applied to detect the change in the composition of $Ni_{0.4}Mg_{0.6}O$ during the pulse experiment. Since there may be a diffraction peak of metallic Ni at 44° near the peak, corresponding to the (200) plane of $Ni_xMg_{1-x}O$, the second strongest peak for the (220) plane of $Ni_xMg_{1-x}O$ was analyzed. The XRD patterns in the range of 60°–64° for $Ni_{0.4}Mg_{0.6}O$ after different pulses of the ethanol–water mixture are given in Fig. 3(b). The lattice parameter of the reduced $Ni_{0.4}Mg_{0.6}O$ was calculated according to the peak position. If the distribution of Ni^{2+} and Mg^{2+} in $Ni_xMg_{1-x}O$ is homogeneous, then the Ni content, x, of such a solid solution can be calculated according to Vegard's law [28]:

$$a_{Ni_xMg_{1-x}O} = xa_{NiO} + (1 - x)a_{MgO} \quad (10)$$

where $a_{Ni_xMg_{1-x}O}$ is the lattice constant of $Ni_xMg_{1-x}O$, and the lattice constants of NiO (a_{NiO}) and MgO (a_{MgO}) were obtained from pure oxides (powder diffraction file (PDF) No. 47–1049 for NiO and PDF No. 45–0946 for MgO). Based on the calculated lattice constants of the reduced $Ni_{0.4}Mg_{0.6}O$, we obtained the Ni contents and degree of reduction of $Ni_{0.4}Mg_{0.6}O$ (Figs. 3(c) and (d)).

The change in the degree of reduction of $Ni_{0.4}Mg_{0.6}O$ is in accordance with the findings from the pulse experiment. In stage I, the degree of reduction of $Ni_{0.4}Mg_{0.6}O$ increases rapidly. The complete oxidation of ethanol is dominant, with the generation of CO_2. In stage II, H_2 is formed consistently in the last three pulses. Simultaneously, oxygen release continues according to the change in the degree of reduction of $Ni_{0.4}Mg_{0.6}O$. In comparison with stage I, the rate of oxygen release in stage II drops, indicating that the oxygen from $Ni_{0.4}Mg_{0.6}O$ participates in the reaction between ethanol and water to produce H_2. H_2 selectivity is increased due to the occurrence of water gas shift. The stoichiometric S/C in ethanol steam reforming (Eq. (1)) is 1.5, which is larger than the S/C in the CLSR and pulse experiment. Therefore, additional oxygen is necessary for stable hydrogen production in stage II. Stage II in the CLSR is carried out as follows:

$$C_2H_5OH + 2H_2O + [O] \rightarrow 2CO_2 + 5H_2 \quad (11)$$

where [O] represents the oxygen from $Ni_xMg_{1-x}O$.

When the active oxygen from $Ni_{0.4}Mg_{0.6}O$ is depleted, the low S/C provides insufficient oxidation capacity for the steam reforming, resulting in decreased selectivity toward H_2 and CO_2 (stage III in the CLSR test). Meanwhile, ethanol is decomposed to carbon, which covers the surface of the OC and leads to deactivation. TGA and O_2-TPO experiments were conducted to verify this process (Fig. S3 in Appendix A). The mass increase at the beginning of the TGA analysis of the reacted $Ni_{0.4}Mg_{0.6}O$ after one cycle can be attributed to the oxidation of Ni (Fig. S3(a)). The subsequent mass loss is in accordance with the peak position of CO_2 in the O_2-TPO, which corresponds to the gasification of the deposited carbon (Fig. S3(b)). The carbon deposition is considered to be the cause of deactivation in stage III. The results also show that the coke generated in the CLSR of ethanol can be eliminated at 600 °C in the regeneration step.

To further investigate the modulation effects of Mg^{2+} on $Ni_xMg_{1-x}O$, H_2-TPR experiments were performed to detect the reactivity of different oxygen species in the solid solution (Fig. 4(a)). No reduction peak was observed over pure bulk MgO up to 900 °C. The reduction peak of NiO is very broad at 200–400 °C. The H_2-TPR profiles of $Ni_xMg_{1-x}O$ mainly consist of a low-temperature reduction peak at around 300 °C and a large reduction peak at 400–800 °C, indicating the existence of two types of oxygen species with different reactivities. Based on the reduction profile of NiO and the structure of $Ni_xMg_{1-x}O$, the low-temperature reduction peak of $Ni_xMg_{1-x}O$ can be attributed to the release of surface oxygen. The large peak in the high-temperature range corresponds to the reduction of Ni^{2+} in the bulk of $Ni_xMg_{1-x}O$ [29]. The temperatures of the different reduction peaks of $Ni_xMg_{1-x}O$ are summarized in Fig. 4(b). The reactivity of the surface oxygen is enhanced with the increase of Ni concentration in $Ni_xMg_{1-x}O$. The reducibility of the metal oxide is related to the band gap between the valence and conduction bands [30]. Closer valence and conduction bands make metal oxides more easily reduced [30]. Previous research indicates that, when the Ni content x is greater than 0.074, the band gap of $Ni_xMg_{1-x}O$ decreases linearly with x [31]. Therefore, the oxygen-release process of $Ni_xMg_{1-x}O$ is inhibited with increased Mg^{2+} content, which aligns with the results from H_2-TPR. Moreover, the coefficient of the Ni^{2+}–Mg^{2+} interdiffusion increases exponentially with the concentration of Ni^{2+} in the air [32]. In conclusion, Ni^{2+} diffusion in $Ni_xMg_{1-x}O$ is suppressed by the lattice confinement of Mg^{2+}. Therefore, the reactivity of bulk oxygen decreases with the enrichment of Mg^{2+} in $Ni_xMg_{1-x}O$, which can be reflected by the increased reduction temperature of bulk oxygen. For the $Ni_{0.2}Mg_{0.8}O$ sample, the reduction temperature for oxygen in the bulk is slightly lower than that of $Ni_{0.4}Mg_{0.6}O$. MgO formed in the surface layer prevents the deeper reduction of bulk $Ni_{0.2}Mg_{0.8}O$, lowering the apparent reduction temperature of bulk oxygen and resulting in a lower degree of reduction (Table 1).

3.4. Proposed reaction pathway over $Ni_xMg_{1-x}O$

To investigate the reaction pathway over $Ni_xMg_{1-x}O$, *in situ* DRIFTS experiments were carried out (Fig. S4 in Appendix A). The spectra collected at different times during the reaction were

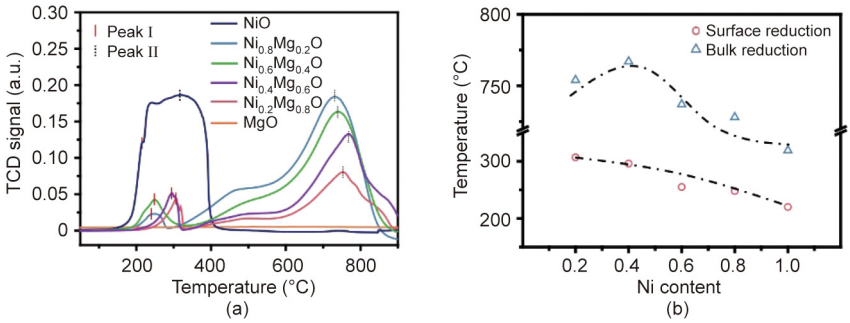

Fig. 4. Temperature-programmed oxygen-release behavior of $Ni_xMg_{1-x}O$. (a) H_2-TPR profiles of NiO, $Ni_xMg_{1-x}O$ (x = 0.2, 0.4, 0.6, and 0.8), and MgO; (b) temperatures for surface oxygen and bulk oxygen release over $Ni_xMg_{1-x}O$ (x = 0.2, 0.4, 0.6, and 0.8) and NiO.

divided into three distinct stages. To observe the changes of the C-containing surface species over $Ni_{0.4}Mg_{0.6}O$, the *in situ* DRIFTS spectra in the range from 2400 to 800 cm^{-1} were obtained, and are presented in Fig. 5.

At the beginning of the reaction, the infrared (IR) peaks of gaseous CO_2 at 2350 cm^{-1} and CO_3^{2-} at 1510 and 1240 cm^{-1} were observed [33]. The generation of CO_2 and CO_3^{2-} can be attributed to the complete oxidation of ethanol by surface oxygen, corresponding to stage I observed in the time-on-stream test. As the reaction proceeds, CO is generated, according to the appearance of the peak at 2170 cm^{-1}. The C–O bond in $CH_3CH_2O^*$ at 1030 cm^{-1} can be seen [34]. The peaks at 1740 and 1580 cm^{-1} are assigned to the C=O bond in CH_3COO^*, which is a characteristic intermediate over Ni-based catalysts in ethanol steam reforming, corresponding to stage II [35]. The IR peaks indicate that the decomposition of ethanol into $CH_3CH_2O^*$ occurs over metallic Ni, and the $CH_3CH_2O^*$ is further oxidized to CH_3COO^*. According to the evidence of the changes in the degree of reduction, water may work collaboratively with the bulk oxygen of $Ni_xMg_{1-x}O$ to oxidize ethanol in stage II. In stage III, the CO_3^{2-} peak disappears gradually, and the intensity of the acetate peak increases. Moreover, the peak at 880 cm^{-1} for the C–H bond in gaseous CH_4 also appears in this stage. The multiple peaks in the range from 1600 to 1400 cm^{-1} correspond to the C–H vibration of the deposited carbon [36]. The changes in the intermediates indicate the occurrence of the decomposition of ethanol to generate CH_4 and carbon in this stage. Due to the low S/C, the oxidation capacity of water is insufficient to convert the surface C-containing species to CO_2. The proposed surface reaction pathway of ethanol for the CLSR of ethanol over $Ni_xMg_{1-x}O$ is in line with the structural evolution of solid solution (Fig. 6).

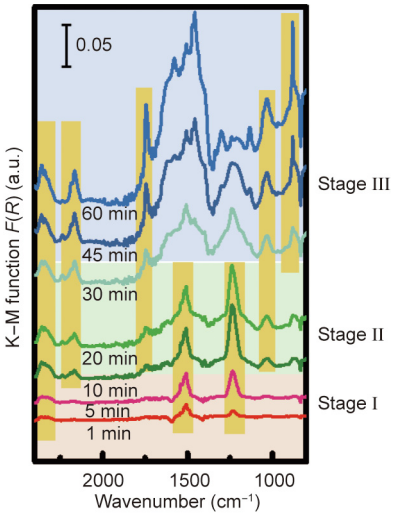

Fig. 5. Changes of C-containing surface species during *in situ* DRIFTS with the ethanol–water mixture (S/C = 1) reacting with $Ni_{0.4}Mg_{0.6}O$ at 400 °C. K–M: Kubelka–Munk.

4. Conclusions

$Ni_xMg_{1-x}O$ solid solution was applied as a novel OC in the CLSR of ethanol for hydrogen production. The oxygen release of $Ni_xMg_{1-x}O$ is regulated with the lattice confinement by Mg^{2+}. As a result, the optimum OC, $Ni_{0.4}Mg_{0.6}O$, was found to exhibit a robust performance toward hydrogen production (4.72 mol of H_2 per mole of ethanol), with an S/C of 1. A three-stage reaction mechanism of the CLSR process was proposed. In stage I, ethanol is completely oxidized by the surface oxygen of $Ni_xMg_{1-x}O$. After the depletion of the surface oxygen and the formation of surface Ni sites, ethanol is oxidized by H_2O and the bulk oxygen from $Ni_xMg_{1-x}O$ collaboratively, achieving the maximum efficiency for hydrogen production in stage II. Without the participation of oxygen species, ethanol steam reforming becomes the dominant process in stage III. The CLSR of ethanol using $Ni_xMg_{1-x}O$ as the OC could potentially reduce the S/C in comparison with conventional steam reforming and achieve renewable hydrogen production from biomass with a minimum external heat supply. This research provides a feasible strategy for the design of a novel OC in diverse chemical looping processes with improved performance and structural stability.

Acknowledgments

This work was supported by National Natural Science Foundation of China (U20B6002, 51761145012, and 21525626) and the Program of Introducing Talents of Discipline to Universities (BP0618007) for financial support.

Compliance with ethics guidelines

Hao Tian, Chunlei Pei, Sai Chen, Yang Wu, Zhjian Zhao, and Jinlong Gong declare that they have no conflict of interest or financial conflicts to disclose.

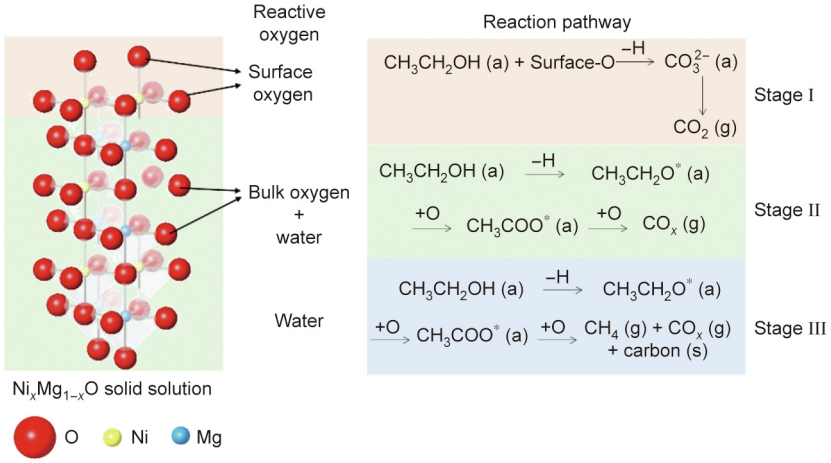

Fig. 6. Schematic illustration of the relationship between oxygen species and the surface reaction pathway over $Ni_xMg_{1-x}O$ during the CLSR of ethanol.

Appendix A. Supplementary data

Supplementary data to this article can be found online at https://doi.org/10.1016/j.eng.2020.08.029.

References

[1] Hosseini SE, Wahid MA. Hydrogen production from renewable and sustainable energy resources: promising green energy carrier for clean development. Renew Sustain Energy Rev 2016;57:850–66.
[2] Liu T, Liu D, Qu F, Wang D, Zhang L, Ge R, et al. Enhanced electrocatalysis for energy-efficient hydrogen production over cop catalyst with nonelectroactive Zn as a promoter. Adv Energy Mater 2017;7(15):1700020.
[3] Liu D, Liu T, Zhang L, Qu F, Du G, Asiri AM, et al. High-performance urea electrolysis towards less energy-intensive electrochemical hydrogen production using a bifunctional catalyst electrode. J Mater Chem A 2017;5(7):3208–13.
[4] Tang C, Qu F, Asiri AM, Luo Y, Sun X. CoP nanoarray: a robust non-noble-metal hydrogen-generating catalyst toward effective hydrolysis of ammonia borane. Inorg Chem Front 2017;4(4):659–62.
[5] Nikolaidis P, Poullikkas A. A comparative overview of hydrogen production processes. Renew Sustain Energy Rev 2017;67:597–611.
[6] Mendiara T, García-Labiano F, Abad A, Gayán P, de Diego LF, Izquierdo MT, et al. Negative CO_2 emissions through the use of biofuels in chemical looping technology: a review. Appl Energy 2018;232:657–84.
[7] Xie Z, Liu Z, Wang Y, Jin Z. Applied catalysis for sustainable development of chemical industry in China. Natl Sci Rev 2015;2(2):167–82.
[8] Rosmaninho MG, Moura FCC, Souza LR, Nogueira RK, Gomes GM, Nascimento JS, et al. Investigation of iron oxide reduction by ethanol as a potential route to produce hydrogen. Appl Catal B Environ 2012;115–116:45–52.
[9] Li D, Li X, Gong J. Catalytic reforming of oxygenates: state of the art and future prospects. Chem Rev 2016;116(19):11529–653.
[10] Yang F, Deng D, Pan X, Fu Q, Bao X. Understanding nano effects in catalysis. Natl Sci Rev 2015;2(2):183–201.
[11] Liu Y, Zhao G, Wang D, Li Y. Heterogeneous catalysis for green chemistry based on nanocrystals. Natl Sci Rev 2015;2(2):150–66.
[12] Dharanipragada NVRA, Galvita VV, Poelman H, Buelens LC, Detavernier C, Marin GB. Bifunctional Co- and Ni-ferrites for catalyst-assisted chemical looping with alcohols. Appl Catal B Environ 2018;222:59–72.
[13] Haribal VP, Chen Y, Neal L, Li F. Intensification of ethylene production from naphtha via a redox oxy-cracking scheme: process simulations and analysis. Engineering 2018;4(5):714–21.
[14] Zeng L, Cheng Z, Fan JA, Fan LS, Gong J. Metal oxide redox chemistry for chemical looping processes. Nat Rev Chem 2018;2(11):349–64.
[15] Cheng Z, Qin L, Fan JA, Fan LS. New insight into the development of oxygen carrier materials for chemical looping systems. Engineering 2018;4(3):343–51.
[16] Chung C, Qin L, Shah V, Fan LS. Chemically and physically robust, commercially-viable iron-based composite oxygen carriers sustainable over 3000 redox cycles at high temperatures for chemical looping applications. Energy Environ Sci 2017;10(11):2318–23.
[17] Han L, Zhou Z, Bollas GM. Model-based analysis of chemical-looping combustion experiments. Part I: structural identifiability of kinetic models for NiO reduction. AIChE J 2016;62(7):2419–31.
[18] Jiang B, Dou B, Wang K, Zhang C, Song Y, Chen H, et al. Hydrogen production by chemical looping steam reforming of ethanol using NiO/montmorillonite oxygen carriers in a fixed-bed reactor. Chem Eng J 2016;298:96–106.
[19] Richardson JT, Scates RM, Twigg MV. X-ray diffraction study of the hydrogen reduction of NiO/α-Al_2O_3 steam reforming catalysts. Appl Catal A Gen 2004;267(1–2):35–46.
[20] Cheng F, Dupont V, Twigg MV. Temperature-programmed reduction of nickel steam reforming catalyst with glucose. Appl Catal A Gen 2016;527:1–8.
[21] Giannakeas N, Lea-Langton A, Dupont V, Twigg MV. Hydrogen from scrap tyre oil via steam reforming and chemical looping in a packed bed reactor. Appl Catal B Environ 2012;126:249–57.
[22] Yoshida T, Tanaka T, Yoshida H, Funabiki T, Yoshida S. Study on the dispersion of nickel ions in the NiO−MgO system by X-ray absorption fine structure. J Phys Chem 1996;100(6):2302–9.
[23] Zhao Y, Hu L, Gao S, Liao M, Sang L, Wu L. One-step self-assembly fabrication of high quality $Ni_xMg_{1-x}O$ bowl-shaped array film and its enhanced photocurrent by Mg^{2+} doping. Adv Funct Mater 2015;25(21):3256–63.
[24] Saitoh T, Kinoshita K, Inada M. Bandgap bowing in $Ni_{1-x}Mg_xO$ alloy. Appl Phys Lett 2018;112(4):041904.
[25] Wei GCT, Wuensch BJ. Composition dependence of ^{63}Ni diffusion in single-crystal NiO–MgO solid solutions. J Am Ceram Soc 1973;56(11):562–5.
[26] de Masi R, Reinicke D, Müller F, Steiner P, Hüfner S. The suppression of NiO reduction in Fe/NiO systems by use of an ultrathin MgO buffer layer, investigated by photoemission and low energy electron diffraction. Surf Sci 2002;516(1–2):L51521.
[27] Huang JJ, Liu W, Yang YH. Phase interactions in Mg–Ni–Al–O oxygen carriers for chemical looping applications. Chem Eng J 2017;326:470–6.
[28] Denton AR, Ashcroft NW. Vegard's law. Phys Rev A 1991;43(6):3161–4.
[29] Hu YH, Ruckenstein E. An optimum NiO content in the CO_2 reforming of CH_4 with NiO/MgO solid solution catalysts. Catal Lett 1996;36(3–4):145–9.
[30] Helali Z, Jedidi A, Syzgantseva OA, Calatayud M, Minot C. Scaling reducibility of metal oxides. Theor Chem Acc 2017;136(9):100.
[31] Niedermeier CA, Råsander M, Rhode S, Kachkanov V, Zou B, Alford N, et al. Band gap bowing in $Ni_xMg_{1-x}O$. Sci Rep 2016;6(1):31230.
[32] Blank SL, Pask JA. Diffusion of iron and nickel in magnesium oxide single crystals. J Am Ceram Soc 1969;52(12):669–75.
[33] Coenen K, Gallucci F, Mezari B, Hensen E. van Sint Annaland M. An *in-situ* IR study on the adsorption of CO_2 and H_2O on hydrotalcites. J CO_2 Util 2018;24:228–39.
[34] Ferencz Z, Erdőhelyi A, Baán K, Oszkó A, Óvári L, Kónya Z, et al. Effects of support and Rh additive on Co-based catalysts in the ethanol steam reforming reaction. ACS Catal 2014;4(4):1205–18.
[35] Zanchet D, Santos JBO, Damyanova S, Gallo JMR, Bueno JMC. Toward understanding metal-catalyzed ethanol reforming. ACS Catal 2015;5(6):3841–63.
[36] Chu PK, Li L. Characterization of amorphous and nanocrystalline carbon films. Mater Chem Phys 2006;96(2–3):253–77.